

## Vibrational Analysis Study of Aluminum Trifluoride Phases

Udo Gross,<sup>†</sup> Stephan Rüdiger,<sup>†</sup> Erhard Kemnitz,<sup>\*,†</sup> Klaus-Werner Brzezinka,<sup>‡</sup>  
Sanghamitra Mukhopadhyay,<sup>§</sup> Christine Bailey,<sup>||</sup> Adrian Wander,<sup>||</sup> and Nicholas Harrison<sup>\*,§,||</sup>

*Institute of Chemistry, Humboldt University, Brook-Taylor-Strasse 2, 12489 Berlin, Germany, Federal Institute of Materials Research and Testing, 12489 Berlin, Germany, Department of Chemistry, Imperial College London, Exhibition Road, London, SW7 2AZ, U.K., and Computational Science and Engineering Department, CCLRC Daresbury Laboratory, Daresbury, Warrington, Cheshire, WA4 4AD, U.K.*

Received: March 27, 2007; In Final Form: May 3, 2007

The vibrational modes of three solid AlF<sub>3</sub> phases ( $\alpha$ ,  $\beta$ , and amorphous high surface area AlF<sub>3</sub>) are investigated. Calculations have been performed using hybrid exchange correlation functionals to determine the equilibrium geometries and  $\Gamma$ -point phonon frequencies for the  $\alpha$ -AlF<sub>3</sub> and  $\beta$ -AlF<sub>3</sub> phases. The calculated optical modes are in excellent agreement with experiment. The IR absorption of the amorphous, glasslike high surface area (HS)-AlF<sub>3</sub> is also discussed. Deconvolution of the broad envelope of IR stretches and bending vibrations identifies the components of the observed broad band. From the IR vibrational spectrum it has been shown that both short-range and medium-range disorder are present within HS-AlF<sub>3</sub>. Structural phase transitions are identified by their phase transition temperature  $T_c$ , measured by thermal analysis.

### 1. Introduction

In studies of structurally distinct aluminum trifluoride phases such as crystalline  $\alpha$ ,  $\beta$ , and the highly disordered high surface area (HS)-AlF<sub>3</sub>, the degree of structural disorder is clearly evident from X-ray diffraction, <sup>27</sup>Al MAS NMR, and scanning electron microscopic (SEM) images as well as from adsorption/desorption isotherms performed by the BET-N<sub>2</sub> method.<sup>1,2</sup> From the combined analysis of the vibrational spectra of both IR and Raman experiments, we hope to gain an understanding of the near range order of distorted aluminum fluoride phases, especially of the amorphous fluoride sample. The hybrid exchange approximation to density functional theory has been used to calculate the equilibrium geometries and  $\Gamma$ -point phonon frequencies of the  $\alpha$ - and  $\beta$ -phases of AlF<sub>3</sub>. Consequently, we can assign the observed vibrational modes of the crystal to particular motions of its constituent octahedra. Although the vibrational spectrum of a matrix-isolated AlF<sub>3</sub> molecule with trigonal planar structure is well-known,<sup>3</sup> an assignment of the vibrational modes of solid AlF<sub>3</sub> has not previously been made. As expected, the IR and Raman data from a crystalline solid are quite different from those of the hexafluoroaluminate ion, AlF<sub>6</sub><sup>3-</sup>.<sup>4</sup>

### 2. Experimental Section

The aluminum fluoride phases were either a commercial product in the case of  $\alpha$ -AlF<sub>3</sub> (Acros, 99.9%) or prepared according to standard procedures and checked by X-ray diffraction (XRD). Additional,  $\alpha$ -AlF<sub>3</sub> was prepared from NH<sub>4</sub>AlF<sub>4</sub> by thermal decomposition at 700 °C in flowing nitrogen. Single crystals of 0.2 × 0.1 mm size were grown from the vapor phase.  $\beta$ -AlF<sub>3</sub> was prepared by thermal decomposition

of  $\alpha$ -AlF<sub>3</sub>·3H<sub>2</sub>O under a self-generating atmosphere. Heating to 400 °C gave a powdered material without single crystals.<sup>5</sup> Amorphous HS-AlF<sub>3</sub> was obtained by sol-gel fluorination and post-fluorination with CHClF<sub>2</sub> according to ref 2. The material is mesoporous with a surface area of 309 m<sup>2</sup>/g. The carbon content is about 0.5%. Fourier transform infrared (FT-IR) spectra were recorded of CsI and KBr disks on a Perkin-Elmer 2000 spectrometer in transmission mode. A 1.5 mg sample was ground with 200 mg of CsI or KBr and pressed. Spectra were measured in the wavenumber ranges of 200–700 and 400–4000 cm<sup>-1</sup> at room temperature. Deconvolution of IR bands was achieved by fitting of superimposed envelopes with Origin software program.

Thermal analysis was carried out with a Netzsch thermoanalyzer STA 409 C Skimmer system. A 40 mg sample was heated in a platinum crucible in a nitrogen gas flow up to 800 °C with a constant heating rate of 10 K/min. The phase transition thermal hysteresis was monitored by the reverse heating-cooling mode.

Laser Raman spectra were recorded from powder samples as well as from a single crystal with an IFS 66v FT-IR spectrometer along with a FRA 106 Raman device (Bruker, Ettlingen, Germany) with excitation by a Nd:YAG laser (DPY 421, Adlas, Lübeck, Germany) at 1064 nm with power levels up to 500 mW, and with a Dilor XY Raman spectrometer (Dilor, Bensheim, Germany) equipped with a nitrogen cooled CCD camera as a detector coupled to a BH-2 microscope (Olympus, Hamburg, Germany) in micromode technique (180° backscatter geometry, objective 50×) with a 514.5 nm excitation line of an ILA 120 argon ion laser (Carl Zeiss, Jena, Germany) with power levels of 10–25 mW into the entrance optics, corresponding to an irradiation density at the sample surface of about 0.1–0.25 mW  $\mu\text{m}^{-2}$ .

### 3. Theory

Theoretical calculations of the equilibrium structure and vibrational modes of  $\alpha$ -AlF<sub>3</sub> and  $\beta$ -AlF<sub>3</sub> were carried out using hybrid exchange density functional theory as implemented within the CRYSTAL program.<sup>12,13</sup> The Bloch orbitals were

\* Corresponding authors. Phone: +493020937555 (E.K.). Fax: +493020937277 (E.K.); +441925603634 (N.H.). E-mail: erhard.kemnitz@chemie.hu-berlin.de (E.K.); nicholas.harrison@imperial.ac.uk (N.H.).

<sup>†</sup> Humboldt University.

<sup>‡</sup> Federal Institute of Materials Research and Testing.

<sup>§</sup> Imperial College London.

<sup>||</sup> CCLRC Daresbury Laboratory.

**TABLE 1: Lattice and Structural Parameters of  $\alpha$ -AlF<sub>3</sub> and  $\beta$ -AlF<sub>3</sub> Phases**

system	cell parameters ( <i>a</i> , <i>b</i> , and <i>c</i> ) (Å)	cell volume (Å <sup>3</sup> )	Al–F (Å)	F–Al–F (deg)	Al–F–Al (deg)
$\alpha$ -AlF <sub>3</sub>	5.042 (4.925)	276.919	1.8164 (1.800)	90.0 (89.9)	161.85 (156.46)
	5.042 (4.925)	(274.054)		90.0 (90.2)	
	12.578 (12.448)				
$\beta$ -AlF <sub>3</sub>	7.036 (6.931)	622.586	1.815 (1.798)	90.2 (90.3)	179.7 (166.4)
	7.261 (7.134)	(593.497)	1.817 (1.800)	90.1 (90.0)	150.8 (148.7)
	12.185 (12.003)		1.818 (1.801)	90.2 (90.2)	179.8 (165.5)
			1.818 (1.801)	89.8 (89.8)	150.8 (148.3)
			1.815 (1.796)	90.0 (89.9)	

expanded in atom centered Gaussian basis sets of triple valence quality. Details of the basis sets used have been reported previously.<sup>14,15</sup> The zone center vibrational modes were computed by numerical differentiation of the analytic gradients and diagonalization of the resultant dynamic matrix. This procedure has recently been used successfully in studies of the vibrations of quartz and corundum.<sup>16,17</sup> An essential prerequisite of the vibrational calculation is the accurate determination of the equilibrium geometry. Optimization of internal coordinates was performed using a modified BFGS algorithm<sup>14,15</sup> until the root-mean-square (rms) and the absolute value of the largest component of the gradient were within 0.00015 and 0.0001 hartree/bohr, respectively, and the rms and the absolute values of the displacements were within 0.015 and 0.01 bohr, respectively. The unit cell parameters were optimized to the same tolerance by successively optimizing the cell parameters and internal coordinates. The splitting of the longitudinal optic (LO) and transverse optic (TO) models due to long-range electrostatic fields has not been computed, and thus for split modes the frequencies reported correspond to TO modes of the crystal. The intensity of IR modes has been evaluated as proportional to the first derivative of the dipole moment with respect to the normal coordinate multiplied by the degeneracy of the mode. The dipole moment derivatives have been calculated from the Born effective charge tensor established from the maximally localized Wannier functions.

## 4. Results and Discussion

**4.1. Structural Information.** In Table 1 we present details of the predicted structure for the bulk unit cells of  $\alpha$ -AlF<sub>3</sub> and  $\beta$ -AlF<sub>3</sub> phase. Experimental values are given in parentheses<sup>18,19</sup> respectively for the  $\alpha$ - and  $\beta$ -phases.

There is one type of octahedron present in  $\alpha$ -AlF<sub>3</sub> but there are two types of octahedra present in  $\beta$ -AlF<sub>3</sub> as shown in Figure 1. These two types have slightly different Al–F distances and F–Al–F angles. The octahedra share corners in an alternating pattern in  $\beta$ -AlF<sub>3</sub> to form six membered and three membered ring structures. We demonstrate later that these differences in structural features produce a rich vibrational spectrum.

**4.2. Rhombohedral  $\alpha$ -AlF<sub>3</sub> Phase.** The thermodynamically stable phase of the aluminum fluorides,  $\alpha$ -AlF<sub>3</sub>, has a rhom-

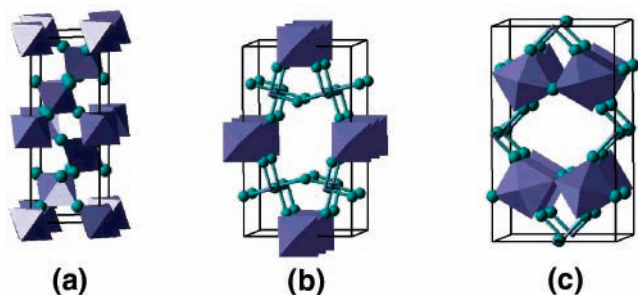


**Figure 1.** (a)  $\alpha$ -AlF<sub>3</sub>. (b)  $\beta$ -AlF<sub>3</sub> with type I octahedra. (c)  $\beta$ -AlF<sub>3</sub> with type II octahedra

bohedral (Figure 1) structure with space group  $R\bar{3}c$  at room temperature.<sup>6</sup> The arrangement of corner shared AlF<sub>6</sub> octahedra undergoes an endothermic phase transition at about 451 °C to the cubic high-temperature AlF<sub>3</sub> phase, isomorphous to ReO<sub>3</sub> discussed later in the text. Daniel et al.<sup>6</sup> have studied the phase transition in detail with the help of Raman absorption bands that exist only in the rhombohedral phase.

According to group theory considerations, 21 optical vibration modes (10 IR active, 4 Raman active, and 7 inactive modes) exist in the low-temperature rhombohedral phase. Fundamental vibrations of symmetry types belonging to the point group  $D_{3d}$  are given in Mulliken notation:

$$A_{1g} + 2A_{2g} + 6E_g + 2A_{1u} + 2A_{2u} + 8E_u$$

among which all E<sub>g</sub> and E<sub>u</sub> modes are doubly degenerate.

The well-resolved peaks in the Raman spectrum (Figure 2) are only observable in spectra from single crystals, i.e., in our small crystallites under a microscope. For truly microcrystalline powders the spectra consist of a broad band in the low-wavenumber region.

The experimentally observed vibration modes are compared with those computed in Table 2. Four of the vibrations are inactive in Raman as well as in IR because of their symmetry. There are also three zero-frequency acoustic modes. The low-frequency Raman active modes denoted as 1 and 2 in Table 2 have temperature-dependent frequencies which disappear at the phase transition temperature  $T_c$  of about 460 °C.<sup>6</sup> Their unusually high intensity is rationalized by the easy excitation of the rotational motion of AlF<sub>6</sub> octahedra in contrast to the very weak stretching and bending lines of Raman modes 3 and 4. This is due to the low polarizability of the rigid fluoride ions, particularly as they are fixed in Al–F–Al bridging positions. None of the four Raman modes is active in the cubic phase. Our data are for room temperature only.

There is excellent agreement between the calculated and measured frequencies. The maximum deviation is 20 cm<sup>-1</sup>,

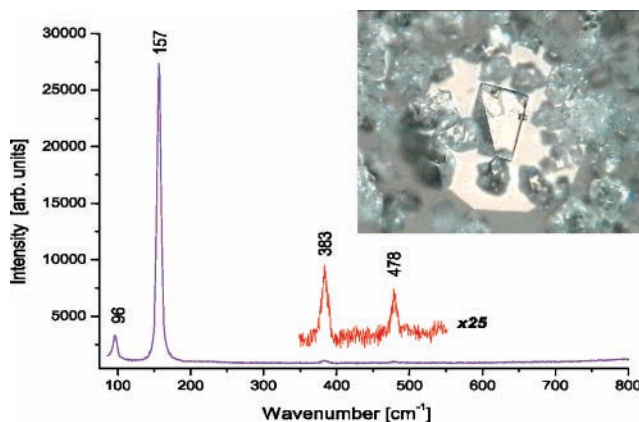


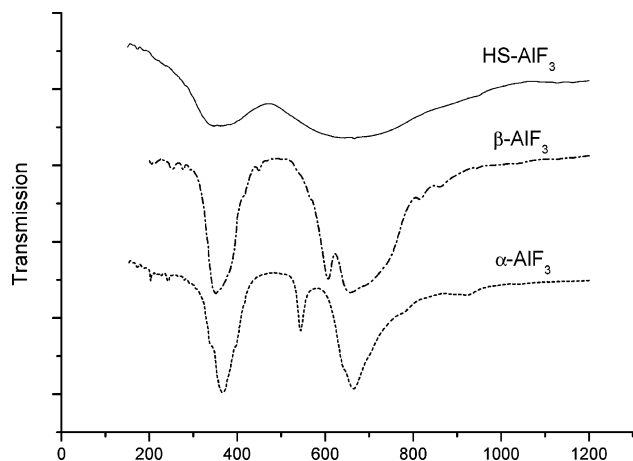
**Figure 2.** Raman spectrum of the  $\alpha$ -AlF<sub>3</sub> rhombohedral phase (inset: crystal).

**TABLE 2: Assignment of Calculated (Athermal Limit) and Experimental (Room Temperature) IR and Raman Modes in  $\alpha$ -AlF<sub>3</sub>**

mode	symmetry type	vibration	frequency (cm <sup>-1</sup> )		relative intensity	
			calcd	exptl	calcd	exptl
Raman						
1	E <sub>g</sub>	rotation of AlF <sub>6</sub>	89.3	96.0		1.0
2	A <sub>1g</sub>	rotation of AlF <sub>6</sub>	136.5	157.2		10.0
3	E <sub>g</sub>	bending Al-F-Al	386.2	382.2		0.1
4	E <sub>g</sub>	stretching Al-F	470.5	478.0		0.01
inactive						
5	A <sub>1u</sub>	bending Al-F-Al	263.5			
6	A <sub>2g</sub>	mixed translation of F	380.8			
7	A <sub>1u</sub>	stretching Al-F-Al	536.9			
8	A <sub>2g</sub>	stretching Al-F	708.0			
IR (TO)						
9	E <sub>u</sub>	bending F-Al-F	246.2	240	2	very weak
10	A <sub>2u</sub>	bending F-Al-F	345.7	340	509	moderate
11	E <sub>u</sub>	translation and bending Al-F-Al	356.5	366	971	very strong
12	E <sub>u</sub>	stretch/bending of F-Al-F/Al-F-Al	537.2	540	65	weak
13	A <sub>2u</sub>	stretching Al-F	641.7	640	521	very strong
14	E <sub>u</sub>	stretching Al-F	646.4	666	1000	very strong

which occurs for the Raman active A<sub>1g</sub> and the IR active E<sub>u</sub> modes. All other differences are within 10 cm<sup>-1</sup>. When comparing theoretical and experimental frequencies, it is important to remember that the theoretical results were calculated at 0 K while the experiments were performed at room temperature. The deviations in the Raman active soft mode frequencies may also arise as the result of the presence of anharmonicity. In general, the computed frequencies are an underestimate of those experimentally measured, examples being small underestimations (less than 6 cm<sup>-1</sup>) in the F-Al-F bending mode (E<sub>u</sub>), the Al-F-Al bending mode (E<sub>g</sub>), and the Al-F stretching mode (A<sub>2u</sub>). One reason for these general underestimations may be the slight overestimation of the equilibrium volume of the crystal by 1%. Frequencies computed at the experimental volume are within 10 cm<sup>-1</sup> of those observed. It is notable that the high intensity of modes 11 and 14 (E<sub>u</sub>) is simply due to the double degeneracy of the mode.

The transmission IR spectra for  $\alpha$ -AlF<sub>3</sub>,  $\beta$ -AlF<sub>3</sub>, and amorphous glasslike HS-AlF<sub>3</sub> phases are shown in Figure 3. The IR spectra of the AlF<sub>3</sub> phases are principally broad, especially the antisymmetric stretching vibrations. The full width at half-height (fwhh) increases very strongly in going from  $\alpha$ -AlF<sub>3</sub> (95 cm<sup>-1</sup>) and  $\beta$ -AlF<sub>3</sub> (170 cm<sup>-1</sup>) to the amorphous metal fluoride glass HS-AlF<sub>3</sub> (400 cm<sup>-1</sup>). The sharp peaks observed in the Raman spectrum confirm that the  $\alpha$ -AlF<sub>3</sub> sample is crystalline. The broadness of the two IR peaks which appear around 350 and

**Figure 3.** Transmission IR spectra of  $\alpha$ -AlF<sub>3</sub>,  $\beta$ -AlF<sub>3</sub>, and amorphous glasslike HS-AlF<sub>3</sub> phases.

650 cm<sup>-1</sup> is due to the overlap of several different modes, as can be seen from Table 2. The spectra of  $\beta$ -AlF<sub>3</sub> and HS-AlF<sub>3</sub> can only be discussed in a qualitative manner due to the large degree of disorder present in these samples. Similar findings have previously been widely discussed not only for fluoride but also for oxide glasses.<sup>7</sup> The most probable reason for the very broad peaks is the overlap of close spectral components related to different vibrations.<sup>8</sup> In addition, the HS-AlF<sub>3</sub> sample consists of nanoparticles, approximately 10 nm in diameter.<sup>1</sup> Inherently, the nanoparticle size effect, i.e., the transition from continuously to discrete energy levels of such small cluster aggregates, contributes to the broadening of the vibrational modes. Boulard et al.<sup>9</sup> have calculated the symmetric bending vibration of Al-F-Al bridging fluorine atoms active in the Raman mode. The deviation of the bending angle from 180° to 140° varies the bending mode frequency by about 100 cm<sup>-1</sup>. A small change in the bond length in disordered M-F compounds of 0.2–0.3 Å splits the IR stretching vibrations, resulting in a number of superimposed absorptions.<sup>10</sup> This explains why only single crystals of high structural purity result in well-resolved Raman spectra. Conversely, microcrystalline powders yield spectra in Raman scattering and IR as broad envelopes containing bands of different origins.

**4.3.  $\beta$ -AlF<sub>3</sub> Phase.** The Raman spectrum of the  $\beta$ -AlF<sub>3</sub> phase is known from previous experimental work with single-crystal  $\beta$ -AlF<sub>3</sub> to be composed of two bands.<sup>9</sup> Our microcrystalline material produced only an unresolved broad band centered at about 140 cm<sup>-1</sup> (Figure 4). The infrared spectrum presented in Figure 3 is different from that of the  $\alpha$ -AlF<sub>3</sub> phase. This is due to different connectivities of the AlF<sub>6</sub> octahedra and an inherently different lattice structure;  $\beta$ -AlF<sub>3</sub> has an orthorhombic structure and space group *Cmcm*.<sup>11</sup> The resulting fundamental modes may be classified as

$$8A_g + 7B_{1g} + 7B_{2g} + 5B_{3g} + 9A_u + 10B_{1u} + 11B_{2u} + 12B_{3u}$$

Twenty-seven of these modes are Raman active modes (8A<sub>g</sub> + 7B<sub>1g</sub> + 7B<sub>2g</sub> + 5B<sub>3g</sub>), 33 are IR active modes (10B<sub>1u</sub> + 11B<sub>2u</sub> + 12B<sub>3u</sub>), and 9A<sub>u</sub> modes are inactive. The lower symmetry and thus inequivalent atomic positions within the  $\beta$ -AlF<sub>3</sub> unit cell generates a larger number of vibrational modes than observed in the  $\alpha$ -AlF<sub>3</sub> phase. The calculated and observed (this work and ref 9) zone center frequencies are presented in Table

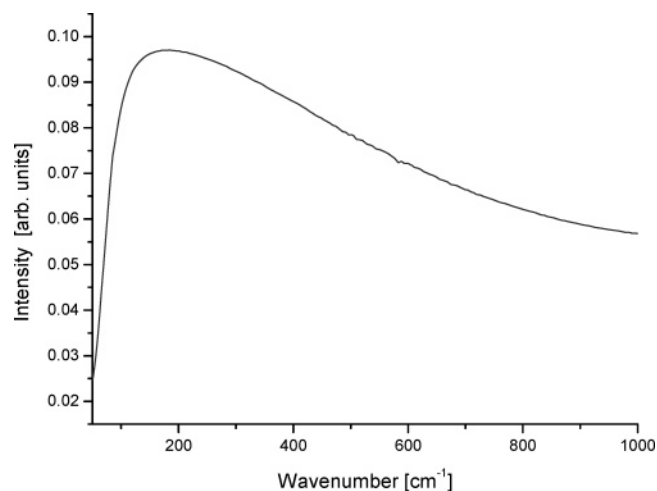


**Figure 4.** Raman spectrum of  $\beta$ -AlF<sub>3</sub> phase.

3. There are many modes that are very close in frequency and almost degenerate due to the close similarities between the two types of octahedra. The theoretical calculations are for an ideal crystal. Therefore, differences between the predicted and observed frequencies are to be expected; nevertheless, the overall agreement between the calculated and experimental ones is reasonable.

The calculated value of the Raman active rotational mode  $A_g$  is underestimated. It reflects the effect of anharmonicity on the soft Raman mode. The effect of temperature and the noncrystalline nature of the experimental sample also contribute to the deviation of the calculated vibrational frequencies from the experimental values. The deviation due to the overestimation of the volume and consequently the underestimation of the frequencies by the B3LYP functional is unlikely to be more than 10 cm<sup>-1</sup>. No Raman active mode in the frequency range of 250–270 cm<sup>-1</sup> has been seen. This may be due to small intensities as obtained for the IR active modes in this region. The intensities of infrared active F–Al–F bending modes are close to zero in this region; hence they cannot be seen experimentally. This also implies that a small dynamic dipole moment is associated with these bending modes.

The first appreciable IR mode, as shown in Figure 3, is an F–Al–F bending mode around 351 cm<sup>-1</sup>. The calculated mode at this frequency is due to the vibration of a bridging F ion and the flexing of F–Al–F angle within an octahedron. The second observed IR mode is located around 600 cm<sup>-1</sup>. This is calculated to be due to the stretching of the F–Al–F angle and is related to the ring structures. The  $B_{2u}$  and  $B_{3u}$  modes in this region, involving the stretching of F–Al–F bonds and bending of the Al–F–Al angle of the ring structure, are not observed. One reason for the absence of these modes may be that the ring structure is distorted. The Al–F stretching modes in the high-frequency regions can be seen, although they are blue-shifted, which may be also for distorted ring structure.<sup>20</sup> The absence of ring structure related modes and the broadening and blue-shifted internal modes indicate that in the noncrystalline sample the Al–F distances vary and that the ring structures are modified from those in a pure  $\beta$ -AlF<sub>3</sub> crystal. It appears that the stretching and ring structure related modes are systematically offset from those computed for ideal  $\beta$ -AlF<sub>3</sub>. From this one can hypothesize that the disorder in the sample is related to distorted ring structure and variation of Al–F bond lengths but not to Al–F–Al bond angles, which is significant.

Analysis of the data in Figure 3 and Tables 2 and 3 enables an understanding of how the vibrational modes differ in different

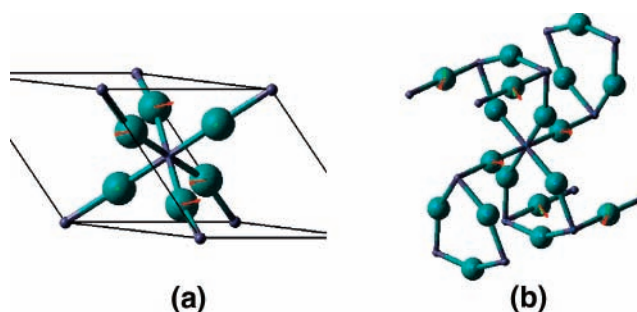


**Figure 5.** F–Al–F bending mode: (a) mode 9 in  $\alpha$ -AlF<sub>3</sub>; (b) modes 45 and 46 in  $\beta$ -AlF<sub>3</sub>.

phases of AlF<sub>3</sub>. The differences in local geometry of the  $\alpha$ -AlF<sub>3</sub> and  $\beta$ -AlF<sub>3</sub> phase are shown in Figure 1 and Table 1. It has been found that not only are there two types of octahedra found in  $\beta$ -AlF<sub>3</sub>, there are also different local geometries as apparent from the differences in Al–F–Al angles. The F–Al–F bending mode at 246 cm<sup>-1</sup> in  $\alpha$ -AlF<sub>3</sub> is blue-shifted to 278 cm<sup>-1</sup> in  $\beta$ -AlF<sub>3</sub>. The eigenvectors of those modes are shown in Figure 5, which shows that these modes belong to similar types of octahedra in two different phases. The change in wavenumber is most likely due to the decrease in size of the octahedra from  $\alpha$ -AlF<sub>3</sub> to  $\beta$ -AlF<sub>3</sub>. The F–Al–F bending  $A_{2u}$  and the double degenerate  $E_u$  modes computed at 345 and 356 cm<sup>-1</sup>, respectively, in  $\alpha$ -AlF<sub>3</sub> are red-shifted to 336 and 350 cm<sup>-1</sup> (the  $B_{3u}$ ,  $B_{2u}$ , and  $B_{1u}$  F–Al–F bending modes) in  $\beta$ -AlF<sub>3</sub>. This is due to the presence of two different types of ring structures. From Figure 2 it can be seen that these modes have broadened at least partly due to the overlap of the different closely spaced modes, as opposed to only being due to a larger degree of disorder in the crystalline  $\beta$ -AlF<sub>3</sub> sample. The calculated mixed mode at 537 cm<sup>-1</sup> for  $\alpha$ -AlF<sub>3</sub> is due to the stretching of F–Al–F bonds and the bending of the Al–F–Al angle. It is blue-shifted to 599.0 cm<sup>-1</sup> in  $\beta$ -AlF<sub>3</sub>. The involvement of members of two different octahedra in the latter case is responsible for the removal of the degeneracy of this mode as well as the blue shift. The additional modes in  $\beta$ -AlF<sub>3</sub> are mainly due to stretching of F–Al–F bonds that connect the two different octahedra in the six membered and four membered ring structures. In this region five modes appear around 639, 640, and 649 cm<sup>-1</sup>. This again broadens the IR peak, although large broadening above 700 cm<sup>-1</sup> may be due to local disorder in the experimental sample.<sup>20</sup>

**4.4. Amorphous HS-AlF<sub>3</sub> Phase.** The amorphous HS-AlF<sub>3</sub> phase is a highly distorted glasslike fluoride in which one cannot expect well-resolved Raman lines (Figure 6).<sup>5</sup> This phase is a product of the recently discovered nonaqueous sol–gel fluorination route to nanosized metal fluorides.<sup>2</sup> The structure, surface properties, and spectroscopic details are studied elsewhere.<sup>21,22</sup> Very recently, Chaudhuri et al.<sup>23</sup> used empirical molecular dynamics simulations (MD) to study the disorder and reactivity of nanostructured AlF<sub>3</sub> units. This simulation suggests that the surfaces are very dynamic on a time scale of picoseconds and with Al–F bonds are continually broken and re-formed. The finite size effect provides not single frequency vibrations but broad normal modes. Unlike in a single crystal of  $\alpha$ -AlF<sub>3</sub>, no phase transition from a rhombohedral to a cubic phase was found in these calculations.

Deconvolution of the broad band around 670 cm<sup>-1</sup> of the Al–F stretch of the amorphous fluoride phase is shown in Figure 7. This principally shows how the experimental envelope can be split off and traced back to six single spectral absorptions to produce a reliable fit. (The real number of single components

TABLE 3: Assignment of Calculated and Experimental IR and Raman Modes in  $\beta$ -AlF<sub>3</sub>

mode	symmetry type	vibration	frequency (cm <sup>-1</sup> )		relative intensity	
			calcd	exptl	calcd	exptl
Raman						
1	B <sub>1g</sub>	rotation of AlF <sub>6</sub>	41.8			
2	A <sub>g</sub>	rotation of AlF <sub>6</sub>	42.3			
3	A <sub>g</sub>	rotation of AlF <sub>6</sub>	53.6	75 <sup>9</sup>		10.0
4	B <sub>2g</sub>	bending F-Al-F	249.0			
5	B <sub>3g</sub>	bending F-Al-F	249.8			
6	A <sub>g</sub>	bending F-Al-F	251.1			
7	B <sub>1g</sub>	bending F-Al-F	251.8			
8	B <sub>1g</sub>	bending F-Al-F	263.4			
9	A <sub>g</sub>	bending F-Al-F	263.5			
10	B <sub>1g</sub>	bending F-Al-F	266.4			
11	B <sub>2g</sub>	bending F-Al-F	267.3			
12	B <sub>3g</sub>	bending F-Al-F	267.4			
13	B <sub>2g</sub>	bending F-Al-F	277.6			
14	A <sub>g</sub>	bending F-Al-F	379.2			
15	B <sub>1g</sub>	bending F-Al-F	379.3			
16	A <sub>g</sub>	bending F-Al-F	391.4			
17	B <sub>2g</sub>	bending F-Al-F	411.1			
18	A <sub>g</sub>	bending Al-F-Al	420.2	411 <sup>9</sup>		3.5
19	B <sub>3g</sub>	stretching Al-F	459.6			
20	B <sub>1g</sub>	stretching Al-F	460.9			
21	B <sub>3g</sub>	stretching Al-F	467.9			
22	B <sub>2g</sub>	stretching Al-F	468.2			
23	B <sub>2g</sub>	stretching F-Al	630.5			
24	B <sub>1g</sub>	stretching F-Al	637.8			
25	A <sub>g</sub>	stretching F-Al	638.2			
26	B <sub>3g</sub>	stretching F-Al	688.4			
27	B <sub>3g</sub>	stretching F-Al	688.6			
inactive						
28	A <sub>u</sub>	rotation of AlF <sub>6</sub>	130.1			
29	A <sub>u</sub>	bending F-Al-F	169.9			
30	A <sub>u</sub>	bending F-Al-F	257.6			
31	A <sub>u</sub>	bending F-Al-F	299.9			
32	A <sub>u</sub>	bending F-Al-F	300.0			
33	A <sub>u</sub>	bending F-Al-F	558.5			
34	A <sub>u</sub>	stretching F-Al-F	626.9			
35	A <sub>u</sub>	stretching F-Al	635.0			
36	A <sub>u</sub>	stretching F-Al	640.6			
IR (TO)						
37	B <sub>1u</sub>	bending F-Al-F	130.2		0	
38	B <sub>2u</sub>	bending F-Al-F	145.3		0	
39	B <sub>1u</sub>	bending F-Al-F	170.0		0	
40	B <sub>3u</sub>	bending F-Al-F	213.9		0	
41	B <sub>2u</sub>	bending F-Al-F	214.0		0	
42	B <sub>3u</sub>	bending F-Al-F	248.8		0	
43	B <sub>2u</sub>	bending F-Al-F	261.7		0	
44	B <sub>3u</sub>	bending F-Al-F	261.9		0	
45	B <sub>2u</sub>	bending F-Al-F	278.4		21	
46	B <sub>3u</sub>	bending F-Al-F	278.5		19	
47	B <sub>3u</sub>	bending F-Al-F	282.3		0	
48	B <sub>1u</sub>	bending F-Al-F	299.6		0	
49	B <sub>1u</sub>	bending F-Al-F	300.3		0	
50	B <sub>2u</sub>	bending F-Al-F	321.1		0	
51	B <sub>3u</sub>	bending F-Al-F	336.0		1091	
52	B <sub>2u</sub>	bending F-Al-F	336.4		1087	
53	B <sub>1u</sub>	bending F-Al-F	351.8	350	1543	very strong
54	B <sub>1u</sub>	bending Al-F-Al	373.9		0	
55	B <sub>3u</sub>	bending F-Al-F	389.3		0	
56	B <sub>3u</sub>	bending and stretching F-Al-F	549.9		0	
57	B <sub>2u</sub>	bending F-Al-F	550.2		0	
58	B <sub>1u</sub>	bending and stretching F-Al-F	558.0		0	
59	B <sub>1u</sub>	bending F-Al-F	586.2		0	
60	B <sub>3u</sub>	bending Al-F-Al/stretching F-Al-F	599.1		1152	
61	B <sub>2u</sub>	bending Al-F-Al/stretching F-Al-F	599.1	600	1183	moderate
62	B <sub>1u</sub>	stretching F-Al-F	627.0		0	
63	B <sub>3u</sub>	stretching F-Al-F	639.3		698	
64	B <sub>1u</sub>	stretching F-Al	639.4		0	
65	B <sub>2u</sub>	stretching F-Al-F	639.5		654	
66	B <sub>3u</sub>	stretching F-Al-F	640.5		3	
67	B <sub>2u</sub>	stretching F-Al-F	641.6		19	
68	B <sub>1u</sub>	stretching F-Al	649.6		1552	
69	B <sub>3u</sub>	bending F-Al-F	650.6	655-750		(broad), very strong

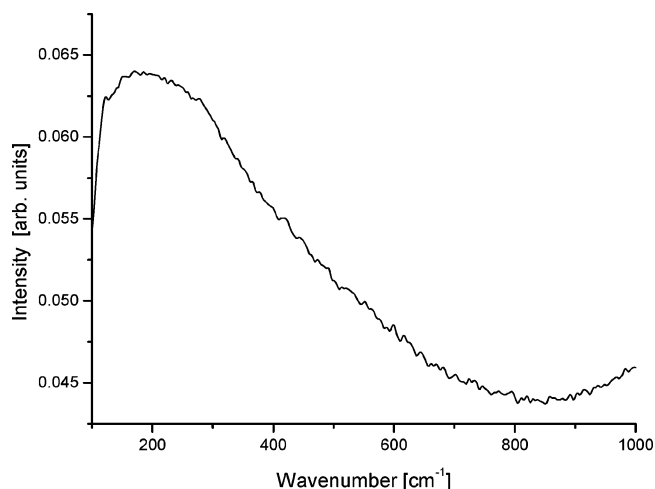


Figure 6. Raman spectrum of the HS- $\text{AlF}_3$  phase.

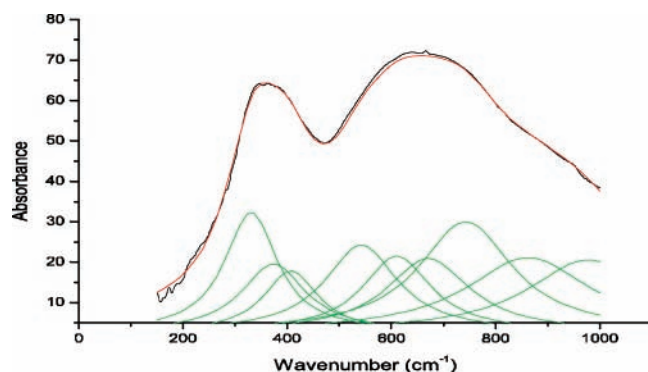


Figure 7. Deconvolution of the IR Al-F stretching absorption of HS- $\text{AlF}_3$ .

contributing to the band width could be much greater than these calculated from the deconvolution modeling.) The maxima occur at the wavenumbers 539, 608, 666, 743, 860, and 977  $\text{cm}^{-1}$ . The occurrence of  $\text{AlF}_3$  species giving rise to such a broad range of vibrational frequencies confirms again the assumption of a spread of Al-F bond lengths. The broad peaks for  $\beta\text{-AlF}_3$  correspond at least partly to the presence of two different sizes of octahedra. It is expected that in high surface area amorphous HS- $\text{AlF}_3$  many more diverse structures are present. In amorphous materials the breakdown of the conservation of wave vector causes all modes which were inactive in either Raman or IR to become active.<sup>20</sup> This will also, in part, contribute to the broadening of the peaks in the vibrational spectrum.

From the assignment of the individual peaks it is observed that HS- $\text{AlF}_3$  consists of both the  $\alpha$ - and  $\beta$ -phases of  $\text{AlF}_3$ . Three modes around 330–400  $\text{cm}^{-1}$  are the superposition of the

doubly degenerate  $E_u$  and  $A_{2u}$  modes of  $\alpha\text{-AlF}_3$  and the  $B_{iu}$  ( $i = 1, 2, 3$ ) modes of  $\beta\text{-AlF}_3$ . The distinct peaks around this region indicate that medium-range order corresponding to the F-Al-F angle distribution within a single octahedron does not vary significantly between different  $\text{AlF}_3$  phases. The peak around 500  $\text{cm}^{-1}$  again indicates the presence of  $\alpha\text{-AlF}_3$  phase within the system. The bending of F-Al-F angles within a particular ring and the associated F-Al stretching mode give rise to peaks above 700  $\text{cm}^{-1}$ . The width of these peaks indicates that in the HS- $\text{AlF}_3$  there is a large degree of disorder within the system.

**4.5. Phase Transitions.** To describe the thermal stability of  $\text{AlF}_3$  phases, phase transition temperatures were determined by differential thermal analysis (DTA) measurements. Accordingly, the room temperature stable  $\alpha\text{-AlF}_3$  phase shows an endothermic transformation peak at 451  $^\circ\text{C}$  in the heating mode of the DTA curve (Figure 8). A large thermal hysteresis of 13  $^\circ\text{C}$  is observed by subsequent cooling of the sample with an exothermic peak at 438  $^\circ\text{C}$ . These values differ by 5 and 10  $^\circ\text{C}$  from those reported in ref 6. The thermogravimetric curve (TG) is expectedly constant over the whole temperature range up to 700  $^\circ\text{C}$  without any weight loss.

The phase transition temperature of  $\beta\text{-AlF}_3$  to  $\alpha\text{-AlF}_3$  is at about 500  $^\circ\text{C}$ . It could not be exactly determined by thermal analysis even when single crystals were used for the measurements.<sup>11</sup>

The transition from amorphous HS- $\text{AlF}_3$  to  $\alpha\text{-AlF}_3$  results in a strong exothermic peak at 545  $^\circ\text{C}$ .<sup>2</sup> The thermal curve in the cooling mode showed no peak corresponding to a phase transition from cubic to rhombohedral  $\text{AlF}_3$ . This is again in agreement with the behavior predicted for nanoscopic  $\text{AlF}_3$  using MD calculations.<sup>23</sup> According to our observations the  $T_c$  value of the HS- $\text{AlF}_3$  transition is not a constant but varies between 498 and 575  $^\circ\text{C}$ , most frequently from 555 to 565  $^\circ\text{C}$ , depending on the sample. This behavior is a consequence of the varying degree of disorder present. Thus, the phase transition temperature,  $T_c$ , together with the closely related enthalpy of transition,  $\Delta H_{T_c}$  (cal  $\text{g}^{-1}$ ), could be a measure for characterization of the amorphous state.

## 5. Conclusions

IR and Raman bands of the  $\alpha\text{-AlF}_3$  and  $\beta\text{-AlF}_3$  phases were assigned to the symmetry types of space group  $R3c$  and  $Cmcm$ , respectively. Eigenvalues and eigenmodes from density functional theory calculations were compared to the experimental data allowing the assignment of given modes to specific motions of the constituent AlF octahedra. The comparison shows very good agreement for  $\alpha\text{-AlF}_3$ . The agreement for  $\beta\text{-AlF}_3$  phase is qualitative because no single-crystal samples were available

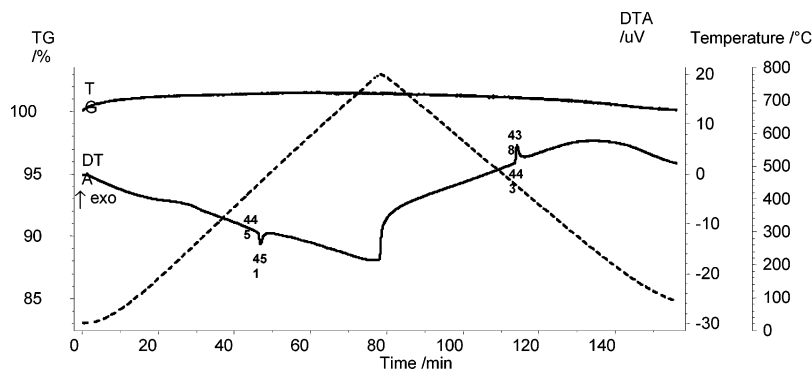


Figure 8. TG curve and thermal analysis curves (DTA) of the single-crystal  $\alpha\text{-AlF}_3$  phase in heating/cooling mode.

for experimental analysis. The comparison shows that the  $\beta$ -AlF<sub>3</sub> sample is disordered and that not only do the Al–F distances vary but also the ring structures are modified. For the HS-AlF<sub>3</sub> sample broad band envelopes representing superimposed spectral components are shown to contribute to the extreme band width. Single absorptions are rationalized by deconvolution fits. The expected access to structure characterization of metal fluorides by vibrational spectra is useful only in a qualitative way, i.e., the wider the band width, the higher the distortion.

**Acknowledgment.** We thank the EU for support in the FUNFLUOS Project, Contract No. NMP3-CT-2004-5005575, within the 6th Framework Programme. We thank Dr. M. Feist for careful performance of thermal analyses.

## References and Notes

- (1) Kemnitz, E.; Gross, U.; Rüdiger, St.; Shekar, C. S. *Angew. Chem., Int. Ed.* **2003**, *42*, 4254.
- (2) Rüdiger, St.; Gross, U.; Feist, M.; Prescott, H. A.; Chandra Shekar, S.; Troyanov, S. I.; Kemnitz, E. *J. Mater. Chem.* **2005**, *15*, 588.
- (3) Snelson, A. *J. Phys. Chem.* **1967**, *71*, 3202.
- (4) Reisfeld, M. J. *Spectrochim. Acta* **1973**, *29A*, 1923.
- (5) Kemnitz, E.; Menz, D. H. *Prog. Solid State Chem.* **1998**, *26*, 97.
- (6) Daniel, P.; Bulou, A.; Rousseau, M.; Nouet, J.; Fourquet, J. L.; Leblanc, M.; Burriel, R. *J. Phys.: Condens. Matter* **1990**, *2*, 5663.
- (7) Almeida, R. M. *J. Non-Cryst. Solids* **1988**, *106*, 347.
- (8) Efimov, A. M. *J. Non-Cryst. Solids* **1997**, *213/214*, 205.
- (9) Boulard, B.; Jacoboni, C.; Rousseau, M. *J. Solid State Chem.* **1989**, *80*, 17.
- (10) Kulikov, A. R.; Ignatyeva, L. N.; Nakadzima, T.; Merkulov, E. B.; Overchuk, E. I. *Glass Phys. Chem.* **1996**, *22*, 15.
- (11) le Bail, A.; Jacoboni, C.; Leblanc, M.; de Pape, R.; Duroy, H.; Fourquet, J. L. *J. Solid State Chem.* **1988**, *77*, 96.
- (12) Saunders, V. R.; Dovesi, R.; Roetti, C.; Orlando, R.; Zicovich-Wilson, C. M.; Harrison, N. M.; Doll, K.; Civalleri, B.; Bush, I. J.; D'Arco, P. H.; Llunell, M. *CRYSTAL 2003, Users's Manual*; University of Torino: Torino, 2004.
- (13) Pascale, F.; Zicovich-Wilson, C. M.; Lopez, F.; Civalleri, B.; Orlando, R.; Dovesi, R. *J. Comput. Chem.* **2004**, *25*, 888.
- (14) Wander, A.; Searle, B. G.; Bailey, C. L.; Harrison, N. M. *J. Phys. Chem. B* **2005**, *109*, 22935.
- (15) Wander, A.; Bailey, C. L.; Searle, B. G.; Mukhopadhyay, S.; Harrison, N. M. *Phys. Chem. Chem. Phys.* **2005**, *7*, 3989.
- (16) Zicovich-Wilson, C. M.; Pascale, F.; Roetti, C.; Saunders, V. R.; Orlando, R.; Dovesi, R. *J. Comput. Chem.* **2004**, *25*, 1873.
- (17) Montanari, B.; Civalleri, B.; Zicovich-Wilson, C. M.; Dovesi, R. *Int. J. Quantum Chem.* **2006**, *106*, 1703.
- (18) Hoppe, R.; Kissel, D. *J. Fluorine Chem.* **1984**, *24*, 327.
- (19) Le Bail, A.; Jacoboni, C.; Beblane, M.; De Pape, R.; Duroy, H.; Fourquet, J. L. *J. Solid State Chem.* **1988**, *77*, 96.
- (20) Sherwood, P. M. A. *Vibrational Spectroscopy of Solids*; Cambridge University Press: Cambridge, 1972.
- (21) Rüdiger, St.; Eltanany, G.; Gross, U.; Kemnitz, E. *J. Sol-Gel Sci. Technol.* **2007**, *41*, 299.
- (22) Rüdiger, St.; Gross, U.; Kemnitz, E. *J. Fluorine Chem.* **2007**, *128*, 353.
- (23) Chaudhuri, S.; Chupas, P.; Morgan, B. J.; Madden, P. A.; Grey, C. P. *Phys. Chem. Chem. Phys.* **2006**, *8*, 5045.